PNAS RESEARCH ARTICLE | NEUROSCIENCE

# Pathogenic variants in autism gene *KATNAL2* cause hydrocephalus and disrupt neuronal connectivity by impairing ciliary microtubule dynamics

Tyrone DeSpenza Jr.[a,b,c,1], Amrita Singh[c,1], Garrett Allington[d,e,1], Shujuan Zhao[f,1], Junghoon Lee[g,1], Emre Kiziltug[c,1], Mackenzi L. Prina[g], Nicole Desmet[g], Huy Q. Dang[g], Jennifer Fields[h], Carol Nelson-Williams[c], Junhui Zhang[c], Kedous Y. Mekbib[c,g], Evan Dennis[e], Neel H. Mehta[e], Phan Q. Duy[a], Hermela Shimelis[i], Lauren K. Walsh[i], Arnaud Marlier[a], Engin Deniz[j], Evelyn M. R. Lake[k], R. Todd Constable[k], Ellen J. Hoffman[a,l], Richard P. Lifton[m], Allan Gulledge[g], Steven Fiering[h], Andres Moreno-De-Luca[i,n], Shozeb Haider[o], Seth L. Alper[p,q], Sheng Chih Jin[f], Kristopher T. Kahle[c,e,q,r,2], and Bryan W. Luikart[g,2]

Affiliations are included on p. 11.

Edited by Lawrence Goldstein, Sanford Consortium for Regenerative Medicine, La Jolla, CA; received August 24, 2023; accepted April 30, 2024

**Enlargement of the cerebrospinal fluid (CSF)–filled brain ventricles (cerebral ventriculomegaly), the cardinal feature of congenital hydrocephalus (CH), is increasingly recognized among patients with autism spectrum disorders (ASD). *KATNAL2*, a member of Katanin family microtubule-severing ATPases, is a known ASD risk gene, but its roles in human brain development remain unclear. Here, we show that nonsense truncation of *Katnal2* (*Katnal2Δ17*) in mice results in classic ciliopathy phenotypes, including impaired spermatogenesis and cerebral ventriculomegaly. In both humans and mice, *KATNAL2* is highly expressed in ciliated radial glia of the fetal ventricular–subventricular zone as well as in their postnatal ependymal and neuronal progeny. The ventriculomegaly observed in *Katnal2Δ17* mice is associated with disrupted primary cilia and ependymal planar cell polarity that results in impaired cilia-generated CSF flow. Further, prefrontal pyramidal neurons in ventriculomegalic *Katnal2Δ17* mice exhibit decreased excitatory drive and reduced high-frequency firing. Consistent with these findings in mice, we identified rare, damaging heterozygous germline variants in *KATNAL2* in five unrelated patients with neurosurgically treated CH and comorbid ASD or other neurodevelopmental disorders. Mice engineered with the orthologous ASD-associated KATNAL2 F244L missense variant recapitulated the ventriculomegaly found in human patients. Together, these data suggest *KATNAL2* pathogenic variants alter intraventricular CSF homeostasis and parenchymal neuronal connectivity by disrupting microtubule dynamics in fetal radial glia and their postnatal ependymal and neuronal descendants. The results identify a molecular mechanism underlying the development of ventriculomegaly in a genetic subset of patients with ASD and may explain persistence of neurodevelopmental phenotypes in some patients with CH despite neurosurgical CSF shunting.**

hydrocephalus | autism | ciliopathy | cerebrospinal fluid dynamics | structural brain disorder

## Significance

We provide evidence that pathogenic variants in the known autism risk gene *KATNAL2* alter cerebrospinal fluid (CSF) dynamics and neuronal connectivity by disrupting ciliary microtubule dynamics in fetal radial glia and their ependymal and neuronal descendants. These results identify a molecular mechanism that may explain the etiology of cerebral ventriculomegaly in genetic subsets of patients with autism spectrum disorders (ASD) and the presence of comorbid ASD and other neurodevelopmental phenotypes in patients with congenital hydrocephalus despite neurosurgical CSF diversion.

Enlargement of the cerebrospinal fluid (CSF)–filled brain ventricles (cerebral ventriculomegaly) is the cardinal feature of congenital hydrocephalus (CH) (1) and is increasingly recognized as an associated structural brain disorder in subsets of psychiatric (2) and neurodevelopmental disorders (NDDs) (3), including schizophrenia (2) and autism spectrum disorder (ASD) (4). The frequent comorbidity of CH and ASD (5–7) is evidenced by the fact that >20% of CH children aged 6 to 17 meet the Autism Behavior Checklist (ABC) diagnostic criteria for ASD (7). Conversely, 13% of children aged 5 to 12 diagnosed with ASD by the Childhood Autism Rating Scale (CARS) also have CH (5–7). The cellular and molecular mechanisms underlying cerebral ventriculomegaly in ASD are poorly understood, as are the ASD-like deficits and other NDDs that can persist in patients with CH despite seemingly adequate neurosurgical CSF shunting (3).

Primary cilia are microtubule-based structures nucleated by the centriole and present on nearly all mammalian cell types, including neural stem cells and their glial and neuronal descendants (8). Primary cilia concentrate signaling molecules of the Hedgehog, WNT, and mTOR signaling pathways to act as signaling hubs in cellular transduction of environmental stimuli (9, 10). Disruption of cilia-based signal transduction causes a pleiotropic group of disorders known as ciliopathies. As primary cilia are ubiquitous, ciliopathies can lead to dysfunction of nearly every organ. Examples of ciliopathy phenotypes include impaired spermatogenesis, cerebral ventriculomegaly, retinal degeneration, polydactyly,

The authors declare no competing interest.

This article is a PNAS Direct Submission.



[1]T.D., A.S., G.A., S.Z., J.L., and E.K. contributed equally to this work.

[2]To whom correspondence may be addressed. Email: kahle.kristopher@mgh.harvard.edu or bryan.w.luikart@dartmouth.edu.

This article contains supporting information online at https://www.pnas.org/lookup/suppl/doi:10.1073/pnas.2314702121/-/DCSupplemental.

Published June 25, 2024.

skeletal malformations, and altered kidney function (11). Brain developmental abnormalities are characteristic of many ciliopathies, reflecting dysfunctions in neurogenesis, neuronal migration, and synaptic connectivity (12, 13). Radial glial cells are primary-cilia-bearing neural stem cells of the ventricular zone (VZ) that give rise to the ependymal cells lining the ventricular system and to cerebral cortical neurons (14–16). The genes that regulate microtubule dynamics and cilia function in human radial glia are poorly understood, as are their contributions to NDDs.

The microtubule-severing ATPase, Katanin, is a heterodimeric complex of catalytic subunit Katanin P60 (KATNA1) and regulatory subunit Katanin P80 (KATNB1) (17). Two lesser characterized KATNA1 P60-like proteins (KATNAL1 and KATNAL2) are predicted to interact with KATNB1 to form additional microtubule-severing enzymes (18). Recent exome sequencing studies in large ASD cohorts have identified pathogenic germline variants in *KATNA1*, *KATNB1*, *KATNAL1*, *KATNAL2,* and the related microtubule severing enzyme *SPAST* (19–22). Interestingly, homozygous missense pathogenic variants in *Kantal1* in mice cause cerebral ventriculomegaly and aberrant neuronal migration (23). However, the roles of katanin and katanin-like proteins in brain development, CSF homeostasis, ventricular morphogenesis, and cortical function remain poorly understood. Moreover, the possible associations between human CH and pathogenic variants in genes encoding Katanin or Katanin-like proteins remain unexamined.

Here, we provide evidence that *KATNAL2* pathogenic variants in mice and humans alter both intraventricular CSF homeostasis and parenchymal neuronal connectivity. In mice, we find that *Katnal2* knockout results in altered planar cell polarity in ventricular ependymal cells, which leads to uncoordinated deflection of motile cilia bundles, abnormal intraventricular CSF currents, and development of ventriculomegaly. We further demonstrate that prefrontal principal neurons in *Katnal2* mutant mice exhibit reduced excitatory/inhibitory synaptic balance and altered firing properties. Consistent with our findings in mice, we identified rare, damaging heterozygous germline variants in *KATNAL2* in five unrelated patients with neurosurgically treated CH and comorbid ASD or other NDDs. These results provide a potential molecular mechanism for the comorbid association of ASD in some neurosurgically treated CH patients, as well as for the presence of cerebral ventriculomegaly in subsets of patients with ASD.

## Results

***Katnal2* Mutant Mice Exhibit Ciliopathy Phenotypes Including Cerebral Ventriculomegaly.** *KATNAL2* transcription yields five splice variants with a shared C-terminal region of 192 residues containing a microtubule-severing AAA ATPase domain ~98% identical between humans and mice. Three additional "long" splice variants of *KATNAL2* contain an N-terminal lissencephaly type-1 homology (LisH) domain. To gain insight into the role of *KATNAL2* in brain development and validate it as a human disease gene, we deleted 17 bp from the mouse *Katnal2* gene using CRISPR-Cas9 in mouse zygotes to knock out *Katnal2* (*Katnal2Δ17*) through nonhomologous end-joining repair, thus eliminating all *Katnal2* long isoforms containing both LisH and AAA ATPase domains (Fig. 1 *A* and *B*). Sanger sequencing distinguished wild-type *Katnal2* and homozygous *Katnal2Δ17* mice (Fig. 1*C*).

Male *Katnal2Δ17* homozygotes were unable to generate litters, but all homozygous mutants had normal lifespans. As mice genetically lacking all *Katnal2* splice variants exhibit multiple spermatogenesis defects, including suppression of centriole duplication-triggered initiation of axoneme growth from the basal body during flagellar development (24), we examined spermatozoa in the testis and epididymis of *Katnal2Δ17* mice. We found impaired spermatozoal maturation with near complete absence of flagella (*SI Appendix*, Fig. S1).

Nissl stained brains of *Katnal2Δ17* homozygous mice aged 4 to 5 mo revealed marked cerebral ventriculomegaly measured at −1.6 to −1.8 mm from bregma [KO = 206.6 ± 337.1 $mm^2$ (n = 11); WT= 51.9 ± 8.5 $mm^2$ (n = 10); $^{****}P < 0.0001$] (Fig. 2 *A–F*). Live-brain MRI in 5-mo-old mice corroborated these results, showing significant communicating (nonobstructive) ventriculomegaly in homozygous *Katnal2 Δ17* mice (134.9 $mm^3$, n = 7) vs. WT littermates (WT = 81.46 $mm^3$, n = 8; $^{**}P = 0.0020$). Six of eight *Katnal2Δ17* homozygous mice were severely hydrocephalic, with ventricular volumes exceeding mean WT ventricular volume by ≥ 2 SD (Fig. 2 *G–I*).

***Katnal2* Is Expressed in Fetal Radial Glial Cells and Perinatal Ependymal Cells.** To gain insight into the molecular mechanisms by which *Katnal2* deletion causes cerebral ventriculomegaly, we first studied *Katnal2* expression in the developing mouse brain using a whole brain single-cell (sc)-RNA sequencing transcriptomic atlas comprising 292,495 cells, including 20 main cell types isolated between E7 and E18 (25) (Fig. 3*A*). Analysis revealed *Katnal2* was most highly expressed in ependymal cells, choroid plexus, and radial glia ($log_2$ fc = 1.69, $P = 2.02 \times 10^{-36}$) (25) (Fig. 3 *B* and *C*). RNAscope in situ hybridization validated these findings in E16.5 mouse brain sections, revealing *Katnal2* expression in $Ki67^+$ proliferating cells and $Map2^+$ differentiated neurons within the VZ/SVZ (Fig. 3*D*).

***Katnal2*-Mutant Ventriculomegaly Is Associated with Altered Primary Cilia, Ependymal Planar Cell Polarity, and Impaired Intraventricular CSF Flow.** Embryonic radial glial cells are a spatiotemporal locus of CH pathogenesis in the human brain and candidate cell types for convergence of CH and ASD risk gene expression (4, 26–28). During embryonic neurogliogenesis, radial glial cells destined to become ependymal cell precursors line the CSF-contacting ventricular walls, where they differentiate into multiciliated ependymal cells (14). Ependymal cilia are polarized through the epithelial plane, and proper localization of ependymal cilia along the ependymal surface is critical for effective CSF flow (29, 30). Primary cilia signaling is thought to establish planar cell polarity and proper arrangement of motile ependymal cilia by integrating SHH/Wnt signaling (31). Based on KATNAL2's microtubule-severing ATPase activity in radial glia, we hypothesized that *Katnal2* loss-of-function (LoF) might disrupt asymmetric distribution of basal body clusters to impair planar cell polarity, thereby decreasing ependymal cilia-polarized CSF flow along the ventricular epithelium.

To test this hypothesis, we performed whole-mount confocal immunofluorescent imaging of lateral ventricle explants to visualize the primary cilia and basal body patch angle of ventricular epithelium in *Katnal2Δ17* mutants and WT controls. To examine primary cilia, we immunostained *Katnal2Δ17* mouse brain at P0/P1 for Arl13b. We noted during sectioning that knockout mice displayed ventriculomegaly, and Arl13b staining revealed longer primary cilia in *Katnal2Δ17* mice than in controls (Fig. 4 *A* and *B*). Due to fragility of the ventriculomegalic neonatal mouse brains during sectioning, we stained whole mounts of adult mouse brains (aged 4 to 5 mo) with anti-γ-tubulin antibodies to detect ciliary basal body clusters and with anti-β-catenin antibodies to detect intercellular junctions of ependymal cell apical domains, in order to quantify basal body cluster angles (Fig. 4 *C* and *D*) (32). We observed loss of basal body translational polarity in both anterodorsal and anteroventral regions of

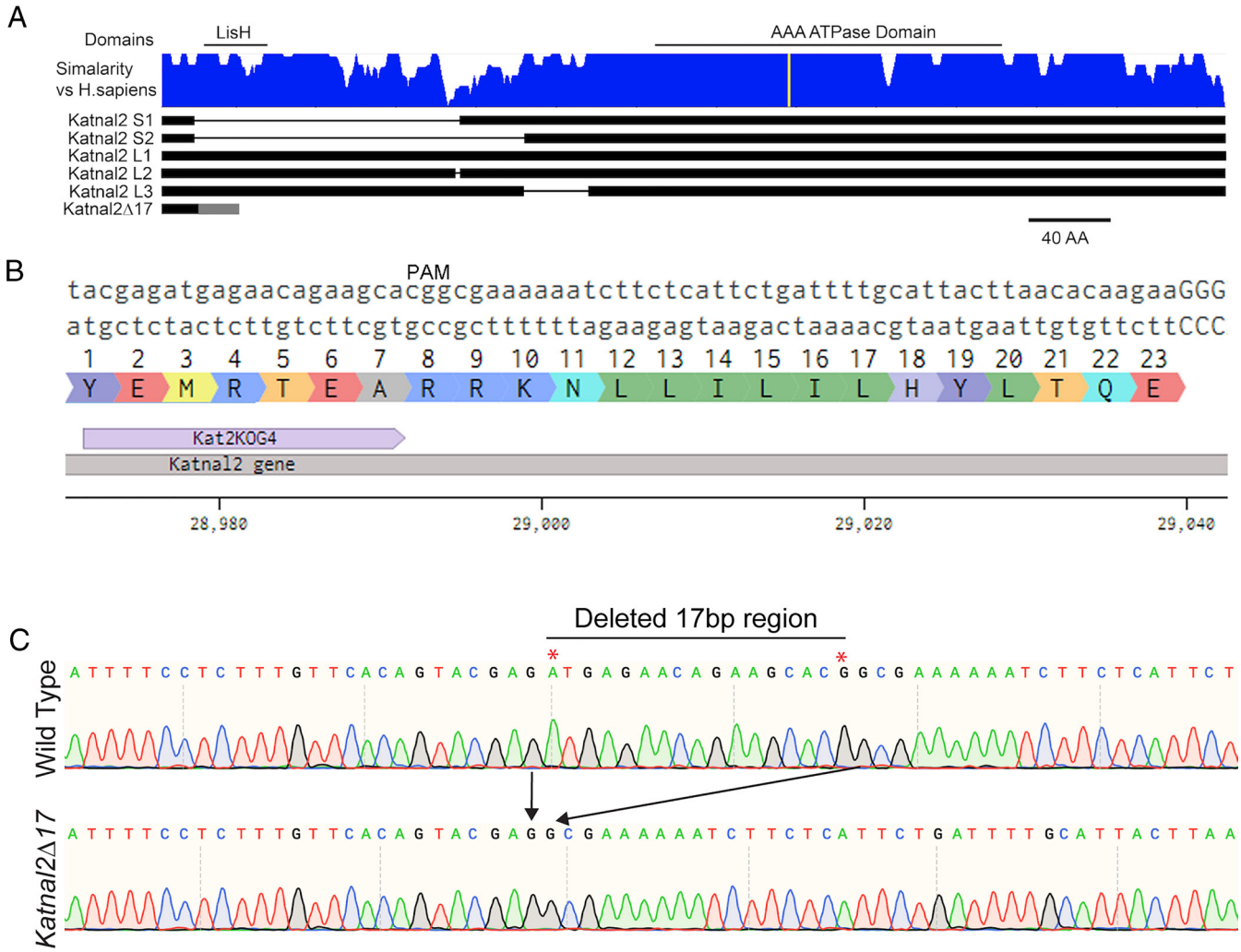


**Fig. 1.** *Katnal2Δ17* mutant mouse creation with CRISPR Cas9-mediated knockout. (*A*) KATNAL2 is predicted to be a microtubule severing enzyme with a LisH domain and an AAA ATPase domain highly conserved between mice and humans. The mouse gene encodes five isoforms: S1, S2, L1, L2, and L3. The *Katnal2Δ17* isoform contains a 17 bp deletion encoding a nonsense truncation in exon 2 shared among all long (L) splice variants. (*B*) Sequence of *Katnal2* exon 2, the translated protein sequence, and the sgRNA "Kat2KOG4" used to generate the *Katnal2Δ17* mice. (*C*) Sanger sequencing chromatograms of WT and *Katnal2Δ17* KO locus confirm 17 bp deletion in exon 2, predicted to knock out all long isoforms.

*Katnal2Δ17* mutants. We also noted impaired basal body cluster polarization on the ependymal surface and qualitatively increased ependymal cilia density in *Katnal2Δ17* mutants. These results suggest that long isoforms of *Katnal2* are required for proper localization of basal body clusters during development of ependymal planar cell polarity, which is critical for proper ciliary orientation.

Because planar cell polarity and uniform cilia bundle orientation are believed necessary for uniform ciliary beating to promote CSF flow, we adopted our optical coherence tomography imaging approach previously validated in *Xenopus* (33) and mice to directly study *Katnal2*-dependent cilia function in ependymal cells (34). In these experiments, ex vivo beating of ependymal cilia can be visualized by movement of polystyrene beads placed on live ventricular explants containing the lateral ventricle. Flow currents that drive bead movement are tracked and calculated as a proxy for microfluidic CSF flow (*Materials and Methods* and Fig. 4 *E* and *F*). Cilia-generated CSF flow in the ependyma of mice aged 4 to 5 mo was significantly lower in the anteroventral region of ventriculomegalic *Katnal2Δ17* mutant mice (9.574 μm/s) than in WT mice (15.44 μm/s; $^{***}P < 0.0005$, n = 4), but not in the anterodorsal region (9.522 μm/s in KO vs. 11.14 μm/s in WT; $P = 0.2099$; n = 4) (Fig. 4 *G* and *H*).

To confirm ciliary motion as requisite for ependymal flow currents in our assay, we applied ciliobrevin, an inhibitor of the motor protein dynein that powers the beating of motile cilia (35), to the anterodorsal region of ependyma of *Katnal2Δ17* mutant and WT mice. We found that the severe reduction of ependymal CSF flow in both mutant and WT was restored by toxin washout (Fig. 4 *I* and *J*). These data suggest that defects in ependymal cilia-generated CSF flow contribute to the pathogenesis of *Katnal2*-mutant ventriculomegaly.

***Katnal2*-Mutant Mice Have Deficits in Cortical Neurophysiology.** The establishment of ependymal planar cell polarity begins prenatally with formation of the primary cilium from the basal body of the radial glia fated to become postnatal ependymal cells (14, 29). This same population of ventricular zone radial glia gives rise to the glutamatergic projection neurons in the prefrontal cortex, including those that project primarily to homologous areas in the contralateral cerebral hemisphere and other cortical targets. Based on these observations, we hypothesized that *Katnal2* depletion, in addition to causing ventriculomegaly by disrupting ependymal cell planar cell polarity and associated cilia-driven intraventricular CSF flow, might also impair the function of neuronal circuits

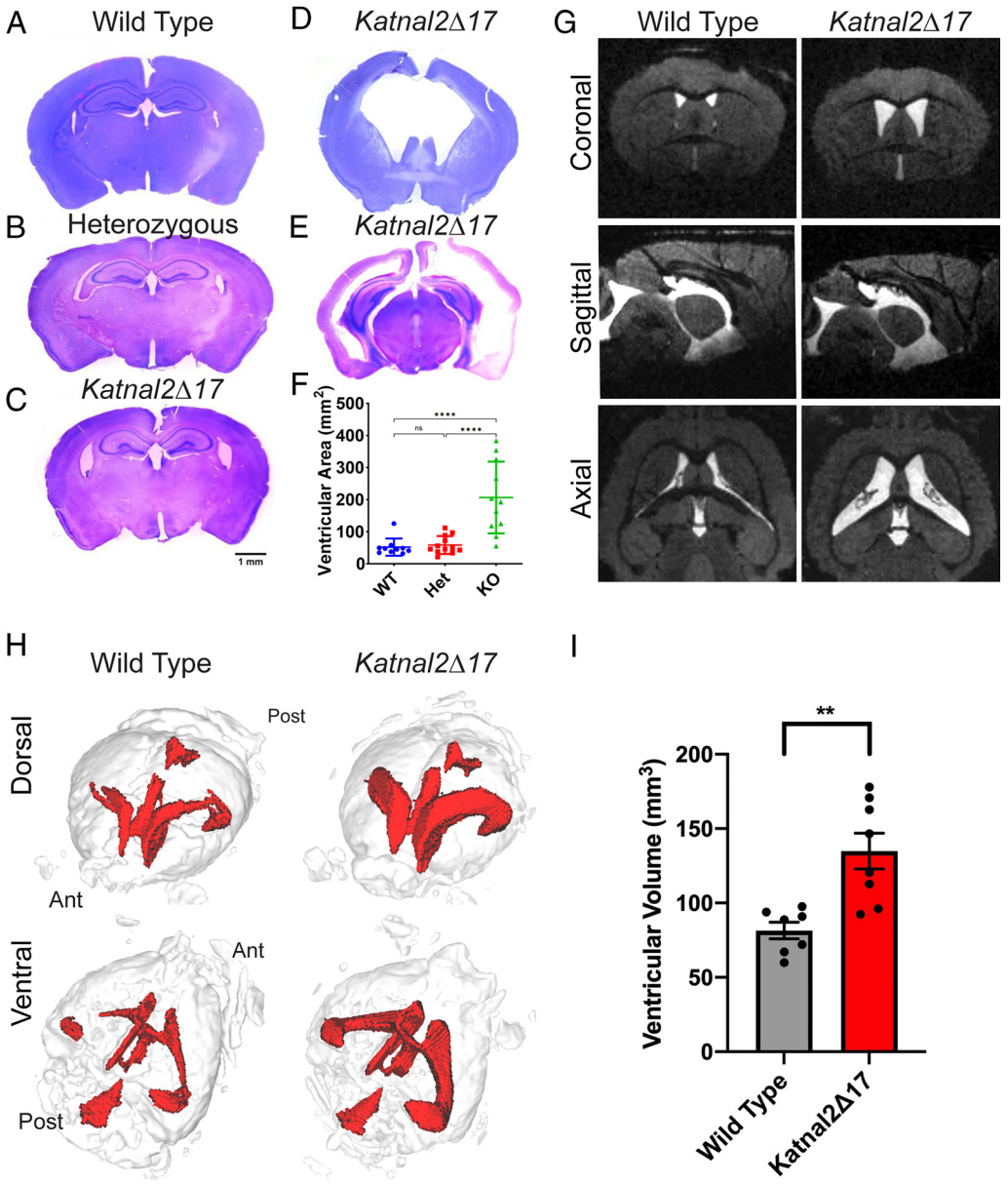


**Fig. 2.** Enlargement of the ventricular area in *Katnal2Δ17* mutant mice. Nissl-stained sections from average wild-type (*A*), heterozygous (*B*), and *Katnal2Δ17* homozygous (*C*) mice. We also observed some *Katnal2Δ17* homozygous mice with more severe hydrocephalus (*D* and *E*). Quantitation of ventricular area in homozygous *Katnal2Δ17* mice (n = 11) greatly exceeded that in *Katnal2 WT* (n = 10) and heterozygous *mice* (n = 10) (*F*). (*G*) Representative in vivo T2 MRIs in coronal, sagittal, and axial planes from a wild-type *Katnal2*$^{+/+}$ mouse and mutant *Kantal2*$^{\Delta 17/\Delta 17}$ littermate at 5 mo of age confirm communicating ventriculomegaly. (*H*) Representative dorsal and ventral views of 3D reconstructions from MRIs as in (*G*) further illustrate the degree of ventriculomegaly. Ant = anterior; Post = posterior. (*I*) Ventricular volumes (mm$^3$) of *Katnal2* WT (gray, n = 7) and *Kantal2Δ17* mice (red, n = 8) at 4 and 5 mo of age were quantitated from MRI data. Means ± SEM; $^{**}P < 0.01$ by the two-tailed *t* test. Means ± SEM; $^{****}P < 0.0001$ by one-way ANOVA.

in the cortical parenchyma, including those implicated in the pathogenesis of ASD.

To determine whether genetic inactivation of *Katnal2* long isoforms resulted in changes in cortical function, we performed whole-cell electrophysiological recording of layer 2/3 pyramidal neurons in P18–P22 prefrontal cortex. We first noted increased input resistance in *Katnal2Δ17* knockout mice [415.0 ± 45.6 MΩ vs. 306.7 ± 6.08 MΩ in WT (both n = 15)]; $P < 0.05$. We also observed decreased frequency of mEPSCs in these neurons (Fig. 5 *A* and *D* and *SI Appendix*, Table S1) without significant change in mEPSC amplitude, rise, width, or decay times in *Katnal2Δ17* mice (Fig. 5 *B* and *D* and *SI Appendix*, Table S1). In contrast, both the mIPSC frequency and amplitude were unaffected in *Katnal2Δ17* mice (Fig. 5*D* and *SI Appendix*, Table S1), although mIPSC rise time was reduced without changes in width or decay time (*SI Appendix*, Table S1). These data suggest that pyramidal neurons of the prefrontal cortex of *Katnal2Δ17* mice have decreased excitatory drive.

To assess intracortical projection neurons, we performed unilateral injection of rAAV2-retro-GFP into the cortices of P0 *Katnal2Δ17* mice to achieve retrograde labeling of callosal projection neurons in the contralateral hemisphere (36). At P20–P22, we identified labeled intratelencephalic projecting pyramidal neurons in layer 5 of the contralateral cortex (Fig. 5 *E* and *F*). Current-clamp recordings of layer 5 *Katnal2Δ17* neurons revealed a resting potential of −75.86 ± 1.05 mV (n = 14), significantly depolarized vs. WT (−80.6 ± 0.61 mV vs. KO; n = 58; $P < 0.001$). After injection of hyperpolarizing current, we observed an increase in the percentage of rebound

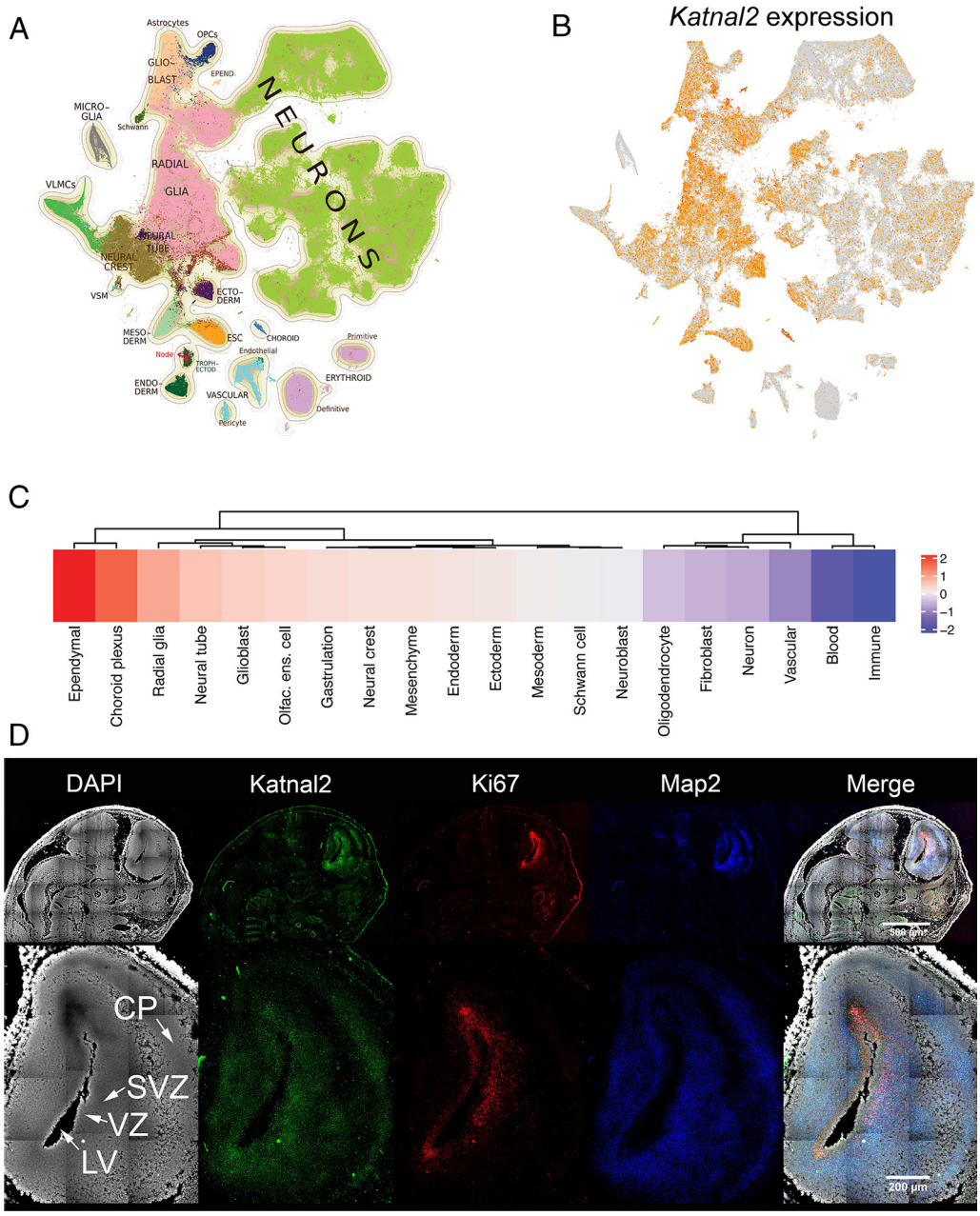


**Fig. 3.** *Katnal2* expression in the developing brain. (*A*) UMAP clustering of mouse fetal brain cells (25), colored by cell type. (*B*) KATNAL2 expression (orange) in the cell clusters shown in (*A*). (*C*) Gene expression heat map showing KATNAL2 expression in the cell types shown in (*A*). (*D*) Multiplexed fluorescent RNAScope of Katnal2 on sagittal sections of E16.5 mouse brain. DAPI counterstain allows anatomical identification of lateral ventricle (LV), ventricular zone (VZ), subventricular zone (SVZ), intermediate zone (not labeled), and cortical plate (CP). A montage of 20× images for Ki67 (red) highlights proliferating VZ cells extending into the SVZ. Map2 mRNA (blue) marks more differentiated neurons of the SVZ and CP. Katnal2 mRNA (green) is most highly expressed in VZ and retains expression in both SVZ and CP. (Scale bar, 200 µm.)

to the steady state (sag %, *SI Appendix*, Table S2). *Katnal2Δ17* neurons also displayed slow after-hyperpolarization potentials with increased magnitude in response to a train of action potentials (Fig. 5*G* and *SI Appendix*, Table S2). *Katnal2Δ17* neurons also displayed action potentials of shorter duration with decreased spike frequency and fast after-hyperpolarization potentials of increased amplitude (Fig. 5*H* and *SI Appendix*, Table S2). The magnitude of injected current required to elicit an action potential (rheobase) was unchanged, as was the action potential amplitude and rise time (*SI Appendix*, Table S2). In summary, electrophysiological recordings indicate that *Katnal2Δ17* pyramidal neurons in the prefrontal cortex display decreased excitatory drive and reduced capability for high-frequency firing, physiological deficits associated with ASD-like alterations in social and cognitive function (37).

***KATNAL2* Variants in Patients with CH and Comorbid Neurodevelopmental Disorders.** Ventriculomegaly is the cardinal feature of CH (1) and is increasingly recognized as an associated structural brain anomaly in ASD (4) and other NDDs (3). *KATNAL2* variants have been previously reported in multiple patients with ASD (38). Based on findings of severe ventriculomegaly and impaired cilia-dependent CSF homeostasis in *Katnal2Δ17* mice, we hypothesized that pathogenic *KATNAL2* variants might also be identified in neurosurgically treated patients with CH.

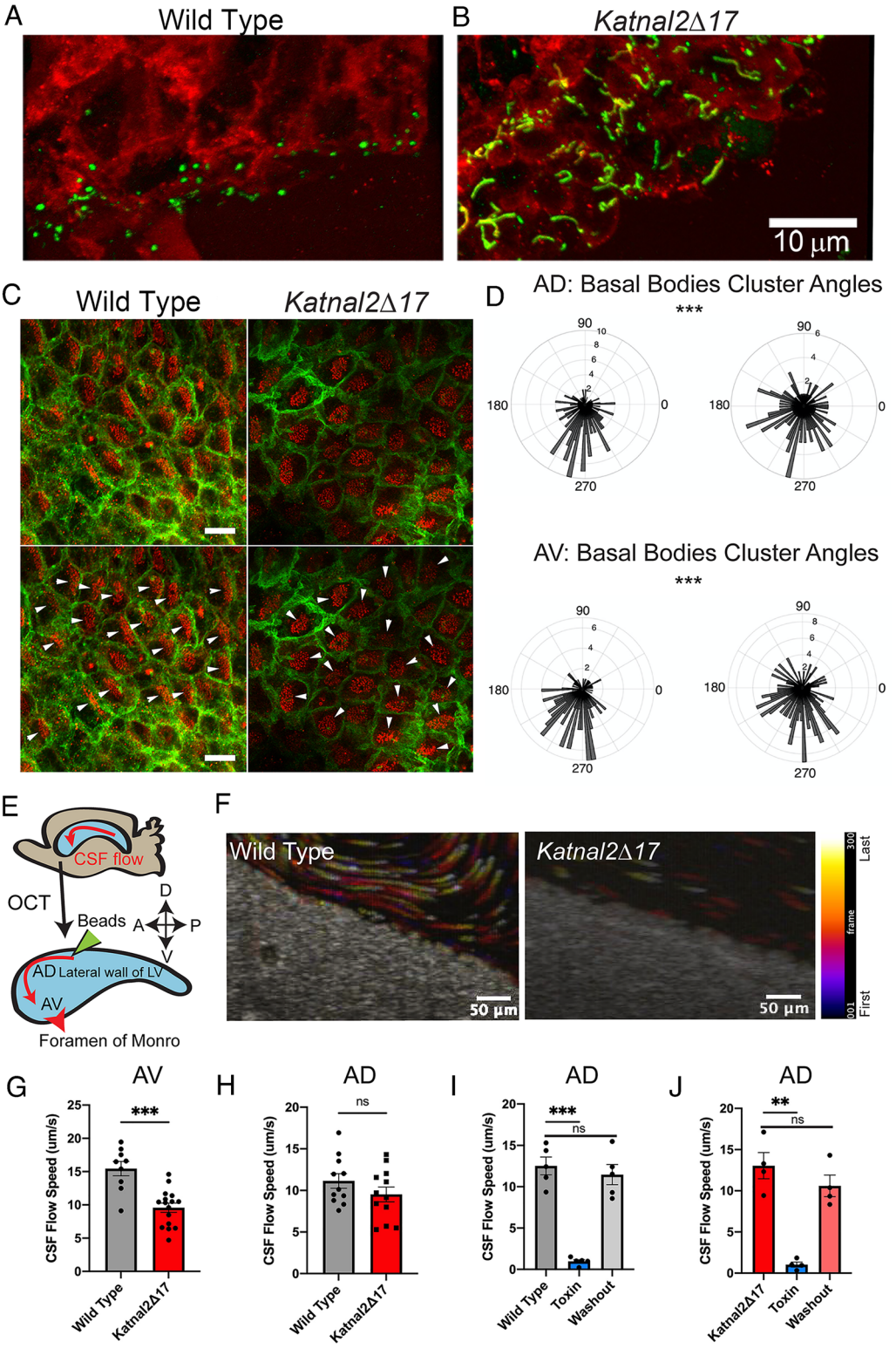


**Fig. 4.** Altered primary cilia, planar cell polarity, and defective CSF flow in *Katnal2Δ17* mice. (*A* and *B*) 3D projection of P0 anteroventral (AV) region stained for ependymal primary cilia using anti-Arl13b (green) outlined by β-catenin (red). (*C*) Whole-mount images from the anterodorsal (AD) area of the lateral ventricle of 4-mo-old mice show basal body clusters expressing γ-tubulin (red) within the apical domains of ependymal cells outlined by β-catenin (green) in wild-type *Katnal2*$^{+/+}$ (*Left*) and mutant *Kantal2*$^{\Delta 17/\Delta 17}$ littermates (*Right*). The cluster orientation of cilia within the ependymal cells is indicated by white arrowheads. (*D*) Basal body cluster angles were plotted on circular maps for both the AD AV areas. Cluster angle distributions differed between *Katnal2*$^{+/+}$ (n = 4) and *Kantal2*$^{\Delta 17/\Delta 17}$ (n = 4) mice. (*E*) Schematic of OCT imaging of microbeads placed onto the AD and AV areas of the lateral wall of lateral ventricle (LV) explants. (*F*) Color-time lapse images from OCT recordings of representative wild-type *Katnal2*$^{+/+}$ (*Left*) and mutant *Katnal2Δ17* littermates (*Right*) aged 4 mo. A temporal color code depicts particle trajectories over time. (*G*) Quantitation of OCT recordings that track flow from individual microbeads reveals decreased velocity of CSF flow in the AV area of mutant *Kantal2*$^{\Delta 17/\Delta 17}$ LV explants (n = 4) relative to *Katnal2*$^{+/+}$ controls (n = 3). (*H*) The AD area of LV explants did not display a change in flow speed. (*I* and *J*) Reversible ciliobrevin inhibition of CSF flow confirms requirement of motile cilia for CSF flow in both WT and mutant mice. Means ± SEM. ***$P < 0.001$; **$P < 0.01$ by the two-tailed *t* test. (n =4). Means ± SEM; ***$P < 0.001$ by the two-tailed *t* test. (Scale bar, 10 μm.)

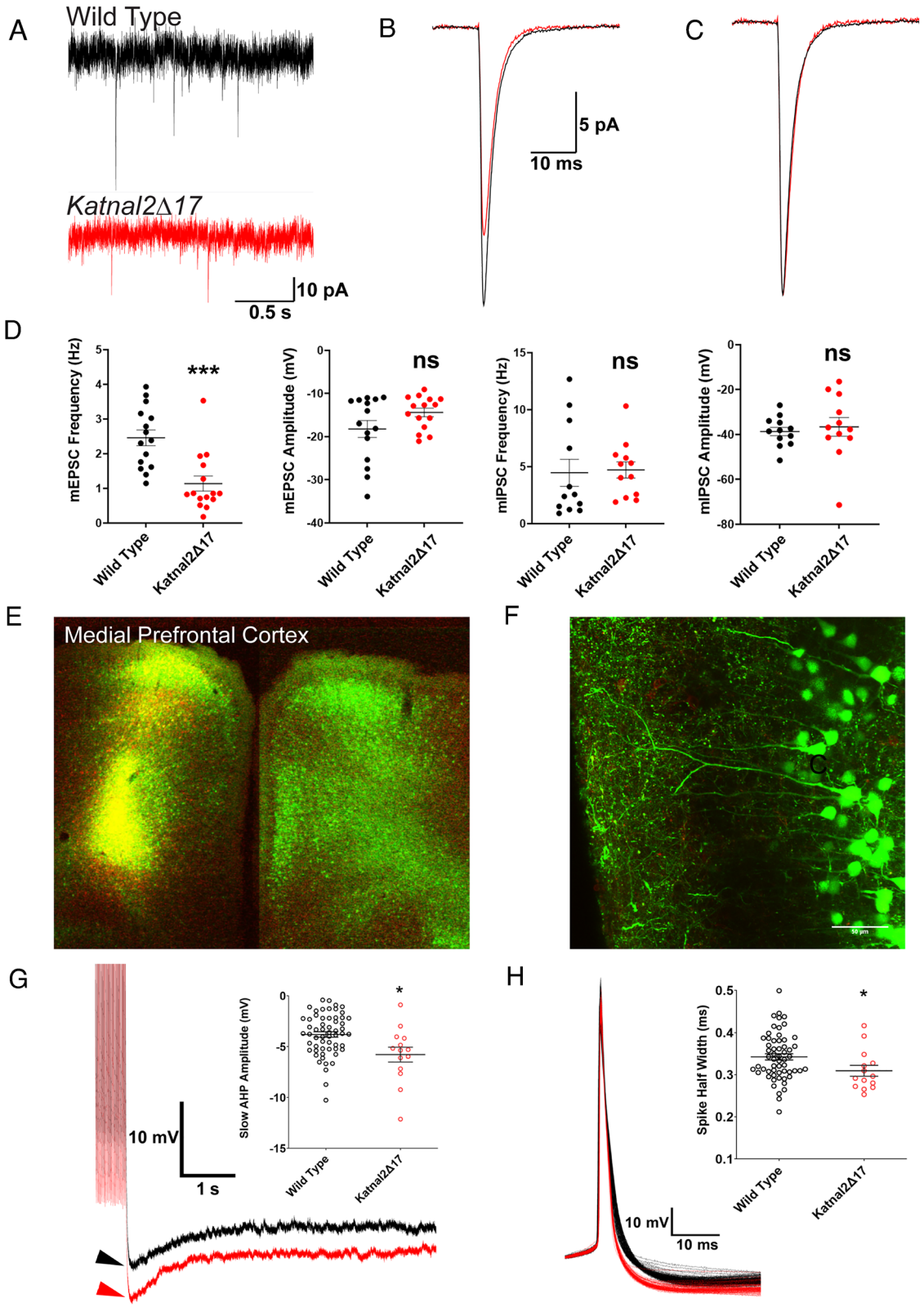


**Fig. 5.** Katnal2 loss leads to decreased frequency of mEPSCs. Whole-cell voltage clamp recording was performed on layer 2/3 pyramidal neurons. (*A*) Representative traces of mEPSCs recorded from P12 acute cortical slices indicate a higher frequency of events in a wild-type neuron than in *Katnal2Δ17* knockout neurons (red). (*B*) Averaged mEPSC waveforms from all captured wild-type (black) and *Katnal2Δ17* neurons (red) displayed nonsignificant increase in amplitude. (*C*) Peak-scaled events from control (black) and KO (red) cells indicate no change in mEPSC kinetics. (*D*) Quantitation of data reveals that *Katnal2* knockout decreases mEPSC frequency with no alteration in mEPSC amplitude or mIPCS frequency or amplitude. (*E*) A mixture of rAAV2-retro-GFP (green) and rAAV8-mCherry-Chrimson (Red) was injected unilaterally into the medial prefrontal cortex of P0 mice. One week after injection, we found both mCherry-chrimson and GFP-positive cells (yellow) in the ipsilateral hemisphere and only GFP-positive callosal projection neurons in the contralateral hemisphere. (*F*) Higher magnification images of an acute brain slice demonstrated specific labeling of layer 5 pyramidal neurons in the contralateral prelimbic cortex. (*G*) Voltage responses to a train of current injections (*Bottom*) recorded in a layer 5 callosal projection neuron in the PFC revealed increased amplitude of the slow AHP in *Katnal2Δ17* knockout (red) vs. wild type (black). The *Inset* shows individual cell data. (*H*) 30 superimposed action potentials in response to short (20 ms) high amplitude (270 pA) current injections. Action potential half-width was reduced in knockout neurons (red; the *Inset* shows individual cell data). Data are means ± SEM. $^{*}P < 0.05$, $^{***}P < 0.001$, by the two-tailed *t* test.

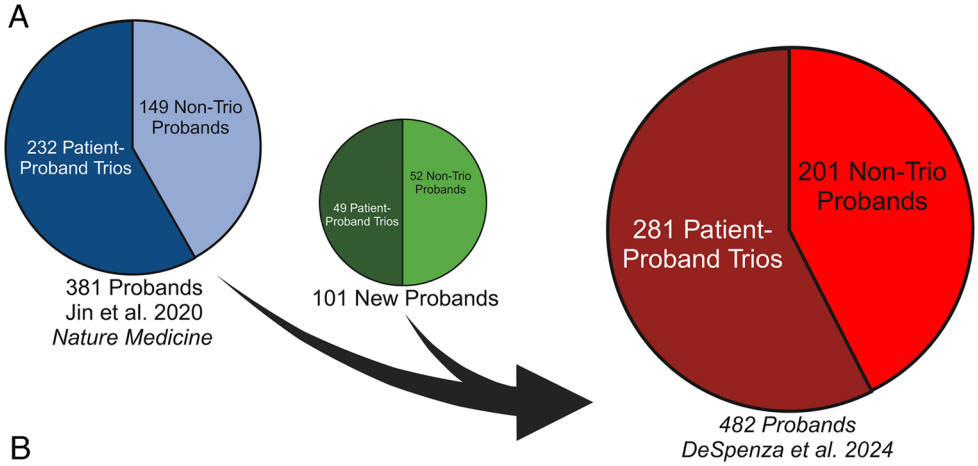


B

| Proband | Sex | Gene | Mutation Type | Position GRCh 37 | AA Change | CADD |
|---|---|---|---|---|---|---|
| NG1535-1 | F | *KATNAL2* | Transmitted | 18:44595878:A:C | p.K233N | 27.3 |
| KCHYD271-1 | F | | Unphased | 18:44625663:G:T | p.D349Y | 28.5 |
| KCHYD246-1 | F | | Transmitted | 18:44589658:C:T | p.R107X | 38.0 |
| KCHYD443-1 | M | | Unphased | 18:44589658:C:T | p.T435P | 23.7 |
| KCHYD115-1 | M | | Transmitted | 18:44627293:G:A | p.D440N | 23.0 |
| KCHYD116-1 | M | *KATNB1* | De novo | 16:57785901:C:T | p.T189M | 30.0 |

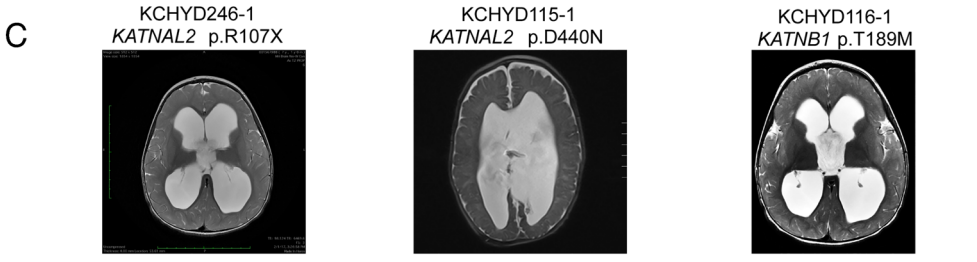


D

| | p.R146 | p.K233 | p.D349 | p.T435 p.D440 | p.T189M |
|---|---|---|---|---|---|
| *H. sapiens* | PDPSERLLKPL | KTLLAKAVATE | KR I L V DLPSRE | LDIVTTADFLDVLTHT | EFPGHTGPVNV |
| *P. troglodytes* | PDPSERLLKPL | KTLLAKAVATE | KR I L V DLPSRE | LDIVTTADFLDVLTHT | EFPGHTGPVNV |
| *A. mississippiensis* | PDPSERLLKPL | KTLLAKAVATE | KR I L V DLPNKG | LDVVTTADFLDVIAHT | EFTGHTGPVNV |
| *X. laevis* | PDPSERLIKPV | KTLLAKAVATE | KR I L V DLPSKE | LETVTTSDFSEVLAHT | ELSEHKGPVN I |
| *B. acutorostrata* | PDPSERLLKPL | KTLLAKAVATE | GQAGHDPPLAA | ---------- | EFPGHTGPVNV |
| *D. rerio* | FTEQERLLKPV | KTMLAKAVATE | K R I L VSLPSA | VGPVTSNDIETALRNT | EFTSHTSAVNV |

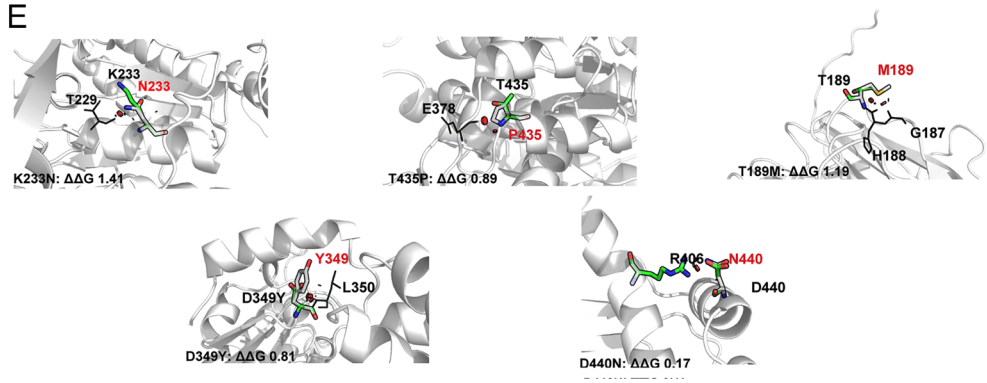


**Fig. 6.** Deleterious, heterozygous *KATNAL2* variants are present in cases of neurosurgically shunted spontaneous human congenital hydrocephalus. (*A*) Flowchart depicting expansion of the clinical cohort used for whole exome sequencing in this study. (*B*) Rare damaging variants in *KATNAL2* and *KATNB1*. (*C*) Representative brain MRI images of individuals KCHYD246-1 and KCHYD115-1 from our CH cohort who harbor heterozygous *KATNAL2* pathogenic variants in the setting of comorbid NDDs (including autism spectrum disorder). (*D*) Evolutionary conservation of heterozygous variants in *KATNAL2* and *KATNB1* identifies several recurrent variants which may mark clinically significant residues. (*E*) In silico biophysical modeling showed that the D-mis variants in *KATNAL2* (p.K233N, p.D349Y, p.T435P, and p.D440N) and *KATNB1* (p.T189M) are predicted to impair protein function.

We therefore analyzed whole-exome sequencing (WES) data from patients with sporadic CH treated by neurosurgical CSF diversion (shunting or endoscopic third ventriculostomy (*Materials and Methods*)) (39). The present study expands the previously published cohort from Jin et al. (39) to include 101 new probands for a total of 1,253 total exomes with 281 proband-parent trios (Fig. 6*A*). We identified five

unrelated probands with rare (MAF < $5 \times 10^{-5}$) LoF or damaging missense heterozygous germline variants in *KATNAL2* (p.R146X, p.D349Y, p.K233N, p.T435P, and p.D440N) (Fig. 6 *B* and *C*). Of these, p.D349Y and p.T435P were unphased and p.R146X, p.K233N, and p.D440N were transmitted from parents without diagnosed CH, autism, or other NDDs. None of these probands had damaging variants in other known CH genes (27, 39).

The variants encoding p.D349Y, p.T435P, and p.D440N are not represented in the Genome Aggregation Database (gnomAD) or other databases. In silico biophysical modeling showed that predicted D-mis variants p.K233N, p.D349Y, p.T435P, and p.D440N each encode substitutions in highly conserved residues predicted to impair function (Fig. 6 *D* and *E*). We also identified a novel damaging de novo pathogenic variant in *KATNAL2* binding partner encoded by *KATNB1* (p.T189M) in a patient with CH and verbal and motor delays. The p.T189M variant in the KATNAL2 binding region of KATNB1 is predicted to be deleterious to protein function (Fig. 6 *D* and *E*).

Interestingly, the *KATNAL2* variant p.D349N found in KCHYD271-1 with CH has been reported in an unrelated proband with ASD (40). Furthermore, the 8-y-old male proband KCHYD115-1 harboring *KATNAL2* p.D440N is nonverbal with poor comprehension skills, irritability, and motor delays. Similarly, KCHYD246-1 harboring *KATNAL2* p.R146X has severe motor and verbal developmental delays. Neurodevelopmental phenotypes of cohort probands harboring deleterious *KATNAL2* variants were unavailable for review. Available MRI brain imaging revealed additional structural brain malformations, including agenesis of the corpus callosum and cerebellum in proband KCHYD115-1 (variant p.D440N), and lissencephaly, corpus callosum dysgenesis and left cerebral atrophy in proband NG1535-1 (variant p.K233N). These results suggest rare, damaging variants in *KATNAL2* cause CH along with other structural brain malformations and neurodevelopmental delays in humans.

**Patient-Associated KATNAL2 Missense Variant Causes Ventriculomegaly In Vivo.** More than 30 *KATNAL2* gene variants have been identified in individuals diagnosed with ASD in the SFARI GENE database (https://gene.sfari.org/database/human-gene/KATNAL2#variants-tab), in addition to the variants we have identified within our CH cohort (Fig. 7*A*). The majority of these *KATNAL2* variants are unphased or transmitted damaging missense variants, which has complicated determination of their pathogenicity.

*KATNAL2* missense variant p.F244L was the first identified *KATNAL2* variant in a large-scale exome sequencing study of individuals diagnosed with ASD (40). To determine whether a patient-associated *KATNAL2* damaging missense variant can cause ventriculomegaly in vivo, we applied CRISPR/Cas9 gene editing to generate a novel humanized mouse model harboring the orthologous mutation *Katna2l*$^{F244L/F244L}$ (*Materials and Methods*). As with *Katnal2Δ17* homozygotes, male *Katnal2*$^{F244L/F244L}$ mice were unable to generate litters (zero litters from six matings), but all homozygous mutants had normal lifespans. Nissl staining of brains from *Katnal2*$^{F244L/F244L}$ homozygous mice aged 3 to 5 mo revealed marked communicating cerebral ventriculomegaly measured at −1.6 to −1.8 mm from bregma [F244L = 123.8 ± 105.1 mm$^2$ (n = 11); WT = 51.25 ± 66.10 mm$^2$ (n = 14); $^*P < 0.05$] (Fig. 7*B*), These findings demonstrate expression of an orthologous patient-associated *KATNAL2* missense variant in mice causes ventriculomegaly in vivo.

## Discussion

Here, we show that nonsense truncation of *Katnal2* (*Katnal2Δ17*) in mice resulting in depletion of all *Katnal2* long isoforms causes impaired spermatogenesis and cerebral ventriculomegaly, classic ciliopathy phenotypes. In both humans and mice, KATNAL2 is highly expressed in ciliated radial glia in the fetal VZ-SVZ and in their postnatal ependymal and neuronal descendants. Ventriculomegaly in *Katnal2Δ17* mice is associated with disrupted ependymal planar cell polarity that results in impaired cilia-generated CSF flow. Radial glia-derived prefrontal pyramidal neurons in ventriculomegalic *Katnal2Δ17* mice exhibit decreased excitatory drive and reduced high-frequency firing. Consistent with these findings in mice, we identified rare, damaging heterozygous germline variants in *KATNAL2* in five unrelated patients with neurosurgically treated CH and comorbid ASD or other NDDs. Finally, we demonstrate that introducing a previously identified ASD-associated *KATNAL2* mutation (40) into mice *Katnal2*$^{F244L/F244L}$ results in ventriculomegaly.

The lack of flagellated spermatozoa is a robust phenotype, previously shown in an independently generated *Katnal2* LoF mouse model lacking all *Katnal2* isoforms. Indeed, *Katnal2* was required in developing spermatozoa for suppression of centriole duplication and initiation of the axoneme from the basal body during spermatid development (24). This spermatogenesis phenotype led to the hypothesis that KATNAL2 function may be targeted to the less-studied microtubules containing delta (*Tubd1*) and epsilon (*Tube1*) tubulins (24, 41). These isoforms are found in centrioles and basal bodies which also form the core structure of spermatocyte flagella.

Ventricular ependymal cilia are polarized through the epithelial plane, and proper localization of ependymal cilia along the ependymal surface is critical for effective CSF flow (29, 30). To our knowledge, the tubulin isoforms that constitute primary ciliary axonemes and the centrioles from which they develop remain incompletely defined. Primary cilia act as a structural hub for SHH signaling and are implicated in WNT/GSK3B signaling (42, 43). Genetic disruption of these pathways impairs microtubule and actin dynamics and repositions centrioles to alter positioning of ependymal cilia, leading to CSF accumulation in the cerebral ventricles (44, 45). Screening NIH/3T3 cells for genes involved in primary cilia function/SHH signaling identified a cluster of centriole genes including *Tubd1*, *Tube1*, and *Katnb1* (41, 46). KATNAL2 is localized to the basal body of motile ependymal cilia in *Xenopus* and its loss resulted in ventriculomegaly (47). In these basal body clusters, zeta-tubulin, an analog of mouse and human TUBD1 was shown to colocalize with epsilon tubulin and to connect the centriole to the apical cytoskeleton (48). These findings prompted our hypothesis that *Katnal2* LoF would disrupt primary cilia and asymmetric distribution of basal body clusters, impairing planar cell polarity, and leading in turn to diminished ependymal cilia-polarized CSF flow along the ventricular epithelium.

Our findings of ventriculomegaly, altered primary cilia and altered ependymal planar cell polarity corroborate our hypothesis and complement similar emerging studies (49). In our hands, commercially available KATNAL2 antibodies produced nonspecific staining, but sc-RNAseq and RNAscope data corroborated a relevant expression pattern. Our observation of increased primary ciliary length and nonuniform deflection of motile cilia bundles in ependymal cells of *Katnal2* KO ventricles suggests a deficit in primary cilia function in these mice. Interestingly, disruption of CSF flow was greatest in the ventral region of the VZ/SVZ, a site most sensitive to embryonic deletion of primary cilia (50). Accordingly, defects in planar cell polarity that impact ventricular cytoarchitecture have also been reported in other hydrocephalic mouse models (29, 30, 32).

From the perspective of brain parenchymal development, impaired primary ciliary signaling resulting from KIF3a dysfunction in dentate granule precursor cells specifically reduces dendritic

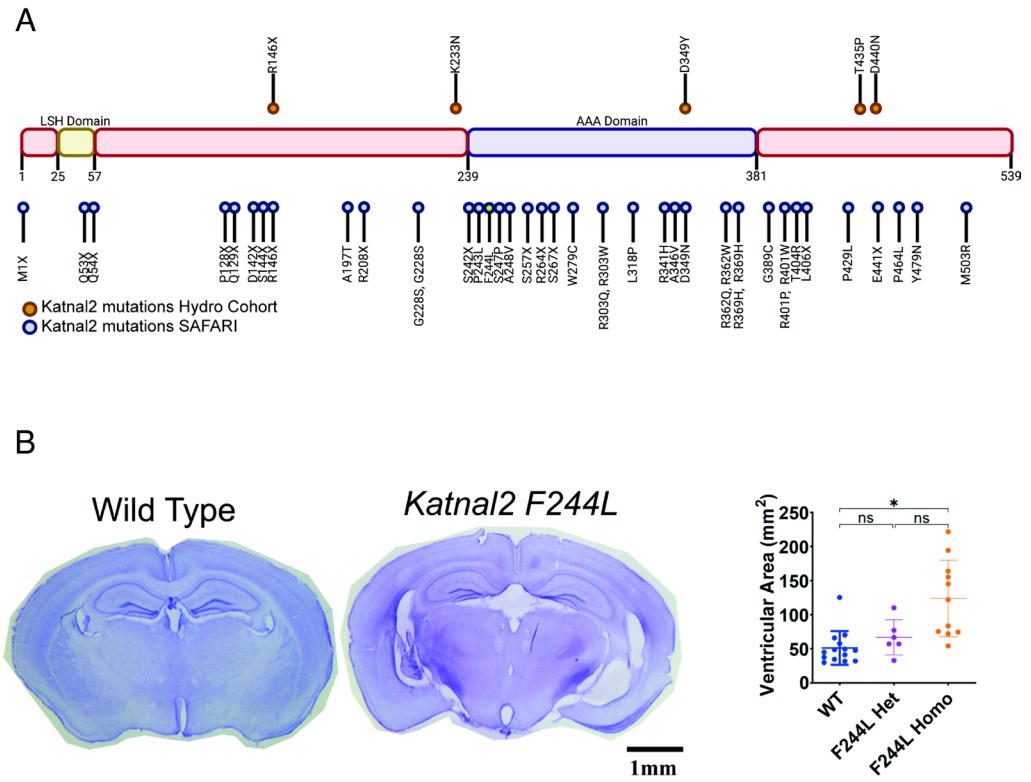


**Fig. 7.** Novel Katnal2 point pathogenic variant mouse recapitulates ventriculomegaly. (*A*) Mapping of all deleterious heterozygous variants in *KATNAL2* from the current cohort (orange) and SAFARI database (blue). (*B*) Representative Nissl stain of coronal brain sections from a wild-type and Katnal2 F244L point mutant mouse with quantitation of ventricular areas reveal Katnal2 F244L mutants have ventriculomegaly.

arborization of, and excitatory synaptic currents onto dentate granule neurons (51). This parallels our present result showing decreased excitatory input onto cortical neurons, and previous results showing decreased arborization of dentate granule neurons after *Katnal2* inactivation (52). Genetic disruption of the related *Katnal1* gene in mice produced behavioral abnormalities, altered neuron migration, decreased dendritic spine density, and ventriculomegaly (23). One *caveat* was that electron microscopic analyses identified deficits in ependymal cell motile cilia in *Katnal1* knockout mice (23). We suggest that impaired primary ciliary signaling in radial glial cells may underlie both cerebral ventriculomegaly and altered cerebral function caused by *Katnal2* LoF. The hypothesis that embryonic primary cilia of radial glia act as a spatiotemporal locus for defects leading to ventriculomegaly and altered development of descendant neurons provides a parsimonious explanation for seemingly disparate effects of altered synaptic connectivity and ventriculomegaly. However, we also note that *KATNAL2* is expressed in both neuronal and ependymal cell descendants of radial glial cells. Therefore, future studies using conditional knockouts are warranted to decouple the primary effect of hydrocephalus from possible cell-autonomous effects on neuronal function.

Our results suggest incomplete penetrance and variable expressivity for some *KATNAL2* variants, a phenomenon well recognized for other CH and ASD risk genes (38). Mechanistic drivers of incomplete penetrance and variable expressivity in this specific context are obscure but could include common genetic or environmental modifiers (38), as well as stochastic components resulting in mosaicism (38). Katanin complex components may share functional scaffolding properties, with up-regulation of other Katanin members compensating for the loss of KATNAL2 in humans, possibly leading to less severe phenotypes. As different KATNAL2 isoforms are expressed in different tissues and at different developmental stages, both the spatiotemporal profile and isoform of the protein containing the variant could affect the phenotype. Recruitment of additional patients will help expand the phenotypic spectrum to allow genotype–phenotype correlations.

The presence of ASD and other comorbid NDDs in neurosurgically treated CH individuals harboring damaging *KATNAL2* variants underscores the importance of our findings that Katnal2 LoF may simultaneously disrupt both CSF homeostasis and normal cortical development. Interestingly, many of the damaging *KATNAL2* variants we identified in hydrocephalic individuals reside in the KATNAL2 primary sequence at or near previously reported ASD-associated *KATNAL2* variants (20, 40). These results also provide a potential molecular mechanism for the comorbid association of ASD in some neurosurgically treated patients with CH, as well as for the presence of cerebral ventriculomegaly in subsets of patients with ASD. A compelling idea arising from these observations is that detection of cerebral ventriculomegaly by fetal MRI or neonatal brain imaging might serve as a radiographic trigger for WES to identify patients harboring ASD-risk genes, allowing for much earlier diagnosis and potentially timely behavioral and physical therapeutic intervention before development of disabling symptoms.

## Materials and Methods

**Animals.** Procedures involving mice were approved and performed following guidelines of the Dartmouth College and Yale University School of Medicine Institutional Animal Care and Use Committee and the Association for the Assessment and Accreditation of Laboratory Animal Care Review Board. All experiments were done in accordance with the regulations set forth by the Yale University animal care and use committee and per the guidelines and regulations in the NIH Guide for the Care and Use of Laboratory Animals.

**CRISPR/Cas9 Generation of *Katnal2* Mutant Mice.** *Katnal2Δ17* and *Katnal2F244L* mice were generated by Luikart and the transgenic core facility at Dartmouth Feiring and Fields. Pathogenic variant of *Katnal2* was performed via CRISPR/Cas9-mediated genome editing essentially as described (53, 54). Please see *SI Appendix* for further details.

**Histological Quantitation of Ventricular Area.** Brains from control and *Katnal2* mutant mice were postfixed in 4% paraformaldehyde for 24 h, washed in 1% PBS, embedded in 2.5% agarose, cut on a vibratome (LeicaVT1000a), and stained with Nissl stain per the manufacturer's protocol (Vector). Sections were imaged with a Leica IC90E camera mounted to a Leica M60 stereomicroscope. Lateral ventricle and brain areas were measured at 0.5 cm anterior to the bregma using Image J. The ratio of ventricular area to brain area was calculated to determine the degree of ventriculomegaly. Pooled data presented as means ± SDs were evaluated using Student's *t* test in Prism version 9.

**Mouse MRI and Quantitation of Ventriculomegaly.** The 11.7 T preclinical Bruker magnet was used to collect Structural MR imaging data (Bruker, Billerica, MA) with an in-house-built saddle coil for optimal whole brain sensitivity. Using our in-house tool [Bioimage Suite (BIS) Web (https://www.bioimagesuite.org)], ventricular volume analyses and 3D reconstructions were done using signal intensity thresholding to delineate the ventricles from surrounding brain tissue (55). Please see *SI Appendix* for further details.

**Single-Cell Atlas Analysis.** The publicly available single-cell atlas of the developing mouse brain by La Manno et al. (25) was used for *Katnal2* gene expression analysis (25). The feature expression plot was created using the interactive wheel plot available at (https://mousebrain.org/development/). The single-cell datasets of early and mid-late human brain development were previously described by Zeng et al. (36) and Ramos et al. (56), respectively. Heatmap values were estimated by averaging expression levels across cell clusters and calculating log2 fold change for each cluster. Visualization of the heatmap was by ComplexHeatmap and pheatmap packages, and bar graphs were created with ggplot2 (57, 58). *P*-values were calculated using the Wilcoxon rank-sum test.

**RNA Scope.** The RNAscope Multiplex Fluorescent assay was performed on fresh frozen embryonic mouse sections from Zyagen. The probes used in this experiment for *Katnal2*, *Ki67*, and *MAP2* were provided by ACDbio. Please see *SI Appendix* for further details.

**Immunohistochemistry.** After perfusion fixation, coronal slices of the cortex (50 μm) were rinsed with 0.4% PBS containing Triton-X (0.4% PBTx) and blocked with 10% donor horse serum in PBS for 1 h at room temperature (RT). Samples were then incubated with primary antibodies for 48 h at 4 °C. Samples were then washed three times for 15 min each in 0.4% PBTx, and incubated with fluorophore-tagged secondary antibodies for 48 h at 4 °C. The immunolabeled samples were washed with 0.4% PBTx and mounted in Vectashield (H-1000, Vector Laboratories). Please see *SI Appendix* for further details.

**Measurement of CSF Flow Rate.** Flow velocimetry used a two-step process of automated particle detection and tracking followed by velocity averaging. Automatic detection of particles and their trajectories was achieved using the Mosaic Particle Tracker plugin in ImageJ (59, 60). Please see *SI Appendix* for further details.

**Electrophysiology.** Mice were anesthetized with intraperitoneal 2% Avertin and subsequently perfused with oxygenated (95%$O_2$/5%$CO_2$) ice-cold cutting solution containing (in mM) 110 choline-Cl, 10 D-glucose, 7 MgCl2, 2.5 KCl, 1.25 $NaH_2PO_4{\cdot}2H_2O$, 0.5 $CaCl_2$, 1.3 Na-ascorbate, and 25 $NaHCO_3$. Whole brains were extracted into ice-cold cutting solution, and coronal 290 μm brain slices were cut with a vibrating microtome and incubated for 30 min at 34 °C in oxygenated (95%$O_2$/5%$CO_2$) artificial cerebral spinal fluid (aCSF) containing (in mM) 125 NaCl, 25 $NaHCO_3$, 2.5 KCl, 1.25 $NaH_2PO_4$, 2.0 $CaCl_2$, 1.0 $MgCl_2$, and 25 D-glucose. ACSF was adjusted to 290 to 295 mOSM by addition of ~4% $H_2O$ by volume. The slices were then stored in oxygenated aCSF at room temperature prior to recording. All recordings were performed at ~37 °C using TC-324B (Warner Instruments). Please see *SI Appendix* for further details.

**Patient Cohort.** All study procedures and protocols were guided by and in compliance with Human Investigation Committee and Human Research Protection Program at Yale University and the Massachusetts General Hospital. All participants provided written, informed consent to participate in accordance with the Declaration of Helsinki. Please see *SI Appendix* for further details.

**Whole-Exome Sequencing and Variant Calling.** Exon capture was performed on genomic DNA samples derived from saliva or blood using the Roche SeqCap EZ MedExome Target Enrichment kit or IDT xGen target capture kit, followed by 101 or 148 base-paired-end sequencing on Illumina platforms. BWA-MEM (61) was applied to align sequence reads to human reference genome GRCh37/hg19. Single-nucleotide variants and small indels were called with GATK HaplotypeCaller (62) and Freebayes (63), and annotated in ANNOVAR (64). Annotated allele frequencies were sourced from data in the Exome Aggregation Consortium (ExAC) (65), gnomAD (v.2.1.1), and Bravo databases (66, 67). Deleteriousness of missense variants was predicted using the MetaSVM and MPC algorithms (D-Mis, defined as MetaSVM-deleterious or MPC-score ≥ 2). Inferred LoF variants consisted of stop-gain, stop-loss, frameshift insertions/deletions, canonical splice site, and start-loss. LoF and D-Mis pathogenic variants were considered damaging (68).

**In Silico Biophysical Modeling.** The structure for human Katanin p60 ATPase-containing subunit A-like 2 (KATL2_HUMAN) was obtained from the Alphafold database (https://alphafold.ebi.ac.uk/) with accession number Q8IYT4. The downloaded structure accounted for residues 1–466. The structure for human Katanin p80 WD40 repeat-containing subunit B1 (KTNB1_HUMAN) was obtained from the Alphafold database with accession number Q9BVA0. The downloaded structure accounted for residues 1 to 655.The pathogenic variants were constructed, and the free energy of change calculated (ΔΔG) in silico using the ICM mutagenesis program (https://www.molsoft.com) (69).

**Data, Materials, and Software Availability.** All study data are included in the article and/or *SI Appendix*.

**ACKNOWLEDGMENTS.** B.W.L. is supported by a grant from the NIH (1R01MH097949). K.T.K. is supported by grants from the NIH (1R01NS109358-01; 1R01NS111029-01A1), Rudi Schulte Organization, Hydrocephalus Association, Simons Foundation, and March of Dimes. T.D. is supported by the NIH Medical Scientist Training Program Training Grant (T32GM007205) and National Institute of Neurological Disorders and Stroke of the NIH under Award Number F31NS115519. Engin Deniz is supported by R01NS127879 and RO1NS111029. A.G. is supported by R01MH124934. *Katnal2Δ17* mice were generated with the Mouse Modeling Shared Resource with support from Dartmouth Cancer Center, NCI P30CA023108, and a grant from the Hitchcock Foundation (to B.W.L.). Confocal imaging was performed at the Imaging Facility on Science Hill at Yale University. The funders had no role in study design, data collection, and analysis, decision to publish or preparation of the manuscript. Certain cartoons and diagrams were generated using BioRender.

Author affiliations: [a]Interdepartmental Neuroscience Program, Yale School of Medicine, Yale University, New Haven, CT 06510; [b]Medical Scientist Training Program, Yale School of Medicine, Yale University, New Haven, CT 06510; [c]Department of Neurosurgery, Yale School of Medicine, Yale University, New Haven, CT 06510; [d]Department of Pathology, Yale School of Medicine, Yale University, New Haven, CT 06510; [e]Department of Neurosurgery, Massachusetts General Hospital, Harvard Medical School, Boston, MA 02115; [f]Department of Genetics, Washington University School of Medicine, St. Louis, MO 63110; [g]Department of Molecular and Systems Biology, Geisel School of Medicine at Dartmouth, Hanover, NH 03755; [h]Department of Microbiology and Immunology, Geisel School of Medicine at Dartmouth, Hanover, NH 03755; [i]Autism and Developmental Medicine Institute, Geisinger, Danville, PA 17821; [j]Department of Pediatrics, Yale University School of Medicine, New Haven, CT 06510; [k]Department of Radiology and Biomedical Imaging, Yale University School of Medicine, New Haven, CT 06520-8042; [l]Child Study Center, Yale School of Medicine, New Haven, CT 06510; [m]Laboratory of Human Genetics and Genomics, The Rockefeller University, New York, NY 10065; [n]Department of Radiology, Diagnostic Medicine Institute, Geisinger, Danville, PA 17821; [o]Department of Pharmaceutical and Biological Chemistry, University College London School of Pharmacy, London WC1N 1AX, United Kingdom; [p]Division of Nephrology and Center for Vascular Biology Research, Beth Israel Deaconess Medical Center, Department of Medicine, Harvard Medical School, Boston, MA 02215; [q]Broad Institute of Harvard and Massachusetts Institute of Technology, Cambridge, MA 02142; and [r]Division of Genetics and Genomics, Boston Children's Hospital, Boston, MA 02115

Author contributions: T.D., K.T.K., and B.W.L. designed research; T.D., A.S., G.A., S.Z., J.L., E.K., M.L.P., N.D., H.Q.D., J.F., C.N.-W., J.Z., K.Y.M., E. Dennis, N.H.M., P.Q.D., H.S., L.K.W., A.M., E. Deniz, E.M.R.L., R.T.C., A.G., A.M.-D.-L., S.H., S.C.J., and B.W.L. performed research; J.F. and S.F. contributed new reagents/analytic tools; T.D., A.S., G.A., S.Z., J.L., E.K., M.L.P., C.N.-W., E. Dennis, H.S., L.K.W., A.M., E. Deniz, E.M.R.L., R.T.C., A.G., A.M.-D.-L., S.H., S.C.J., K.T.K., and B.W.L. analyzed data; and T.D., A.S., G.A., S.Z., J.L., E.K., E.J.H., R.P.L., S.L.A., S.C.J., K.T.K., and B.W.L. wrote the paper.

1. K. T. Kahle, A. V. Kulkarni, D. D. Limbrick Jr., B. C. Warf, Hydrocephalus in children. *Lancet* **387**, 788–799 (2016).
2. P. Svancer, F. Spaniel, Brain ventricular volume changes in schizophrenia. A narrative review. *Neurosci. Lett.* **759**, 136065 (2021).
3. J. Riva-Cambrin *et al.*, Impact of ventricle size on neuropsychological outcomes in treated pediatric hydrocephalus: An HCRN prospective cohort study. *J. Neurosurg. Pediatr.* **29**, 245–256 (2022).
4. T. DeSpenza Jr. *et al.*, PTEN mutations in autism spectrum disorder and congenital hydrocephalus: Developmental pleiotropy and therapeutic targets. *Trends Neurosci.* **44**, 961–976 (2021).
5. H. K. Ryland, M. Hysing, M. B. Posserud, C. Gillberg, A. J. Lundervold, Autism spectrum symptoms in children with neurological disorders. *Child Adolesc. Psychiatry Ment. Health* **6**, 34 (2012).
6. E. Fernell, C. Gillberg, L. von Wendt, Autistic symptoms in children with infantile hydrocephalus. *Acta Paediatr. Scand.* **80**, 451–457 (1991).
7. B. Lindquist, G. Carlsson, E. K. Persson, P. Uvebrant, Behavioural problems and autism in children with hydrocephalus: A population-based study. *Eur. Child Adolesc. Psychiatry* **15**, 214–219 (2006).
8. A. Louvi, E. A. Grove, Cilia in the CNS: The quiet organelle claims center stage. *Neuron* **69**, 1046–1060 (2011).
9. K. H. Elliott, S. A. Brugmann, Sending mixed signals: Cilia-dependent signaling during development and disease. *Dev. Biol.* **447**, 28–41 (2019).
10. K. I. Hilgendorf, C. T. Johnson, P. K. Jackson, The primary cilium as a cellular receiver: Organizing ciliary GPCR signaling. *Curr. Opin. Cell Biol.* **39**, 84–92 (2016).
11. Y. H. Youn, Y. G. Han, Primary cilia in brain development and diseases. *Am. J. Pathol.* **188**, 11–22 (2018).
12. J. P. Baudoin *et al.*, Tangentially migrating neurons assemble a primary cilium that promotes their reorientation to the cortical plate. *Neuron* **76**, 1108–1122 (2012).
13. V. V. Chizhikov *et al.*, Cilia proteins control cerebellar morphogenesis by promoting expansion of the granule progenitor pool. *J. Neurosci.* **27**, 9780–9789 (2007).
14. N. Spassky *et al.*, Adult ependymal cells are postmitotic and are derived from radial glial cells during embryogenesis. *J. Neurosci.* **25**, 10–18 (2005).
15. X. Qian *et al.*, Timing of CNS cell generation: A programmed sequence of neuron and glial cell production from isolated murine cortical stem cells. *Neuron* **28**, 69–80 (2000).
16. S. C. Noctor, A. C. Flint, T. A. Weissman, R. S. Dammerman, A. R. Kriegstein, Neurons derived from radial glial cells establish radial units in neocortex. *Nature* **409**, 714–720 (2001).
17. F. J. McNally, R. D. Vale, Identification of katanin, an ATPase that severs and disassembles stable microtubules. *Cell* **75**, 419–429 (1993).
18. J. E. M. Dunleavy, A. E. O'Connor, H. Okuda, D. J. Merriner, M. K. O'Bryan, KATNB1 is a master regulator of multiple katanin enzymes in male meiosis and haploid germ cell development. *Development* **148**, dev199922 (2021).
19. I. Iossifov *et al.*, The contribution of de novo coding mutations to autism spectrum disorder. *Nature* **515**, 216–221 (2014).
20. S. J. Sanders *et al.*, De novo mutations revealed by whole-exome sequencing are strongly associated with autism. *Nature* **485**, 237–241 (2012).
21. H. A. Stessman *et al.*, Targeted sequencing identifies 91 neurodevelopmental-disorder risk genes with autism and developmental-disability biases. *Nat. Genet.* **49**, 515–526 (2017).
22. A. J. Willsey *et al.*, Coexpression networks implicate human midfetal deep cortical projection neurons in the pathogenesis of autism. *Cell* **155**, 997–1007 (2013).
23. G. Banks *et al.*, A missense mutation in Katnal1 underlies behavioural, neurological and ciliary anomalies. *Mol. Psychiatry* **23**, 713–722 (2018).
24. J. E. M. Dunleavy *et al.*, Katanin-like 2 (KATNAL2) functions in multiple aspects of haploid male germ cell development in the mouse. *PLoS Genet.* **13**, e1007078 (2017).
25. G. La Manno *et al.*, Molecular architecture of the developing mouse brain. *Nature* **596**, 92–96 (2021).
26. S. Jin *et al.*, Inference and analysis of cell-cell communication using Cell Chat. *Nat. Commun.* **12**, 1088 (2021).
27. C. G. Furey *et al.*, De novo mutation in genes regulating neural stem cell fate in human congenital hydrocephalus. *Neuron* **99**, 302–314.e304 (2018).
28. P. Q. Duy *et al.*, Brain ventricles as windows into brain development and disease. *Neuron* **110**, 12–15 (2022).
29. Z. Mirzadeh, Y.-G. Han, M. Soriano-Navarro, J. M. García-Verdugo, A. Alvarez-Buylla, Cilia organize ependymal planar polarity. *J. Neurosci.* **30**, 2600–2610 (2010).
30. B. Guirao *et al.*, Coupling between hydrodynamic forces and planar cell polarity orients mammalian motile cilia. *Nat. Cell Biol.* **12**, 341–350 (2010).
31. S. Wang, J. Hu, Z. Dong, From primary cilia and planar cell polarity to kidney injury and repair. *Nephron* **147**, 721–724 (2023).
32. M. Takagishi *et al.*, Daple coordinates planar polarized microtubule dynamics in ependymal cells and contributes to hydrocephalus. *Cell Rep.* **20**, 960–972 (2017).
33. P. Date *et al.*, Visualizing flow in an intact CSF network using optical coherence tomography: Implications for human congenital hydrocephalus. *Sci. Rep.* **9**, 6196 (2019).
34. P. Q. Duy *et al.*, Impaired neurogenesis alters brain biomechanics in a neuroprogenitor-based genetic subtype of congenital hydrocephalus. *Nat. Neurosci.* **25**, 458–473 (2022).
35. D. H. Roossien, K. E. Miller, G. Gallo, Ciliobrevins as tools for studying dynein motor function. *Front Cell Neurosci.* **9**, 252 (2015).
36. S. I. Ramos *et al.*, An atlas of late prenatal human neurodevelopment resolved by single-nucleus transcriptomics. *Nat. Commun.* **13**, 7671 (2022).
37. S. B. Nelson, V. Valakh, Excitatory/inhibitory balance and circuit homeostasis in autism spectrum disorders. *Neuron* **87**, 684–698 (2015).
38. B. S. Abrahams, D. H. Geschwind, Advances in autism genetics: On the threshold of a new neurobiology. *Nat. Rev. Genet* **9**, 341–355 (2008).
39. S. C. Jin *et al.*, Exome sequencing implicates genetic disruption of prenatal neuro-gliogenesis in sporadic congenital hydrocephalus. *Nat. Med.* **26**, 1754–1765 (2020).
40. S. De Rubeis *et al.*, Synaptic, transcriptional and chromatin genes disrupted in autism. *Nature* **515**, 209–215 (2014).
41. G. G. Stathatos, J. E. M. Dunleavy, J. Zenker, M. K. O'Bryan, Delta and epsilon tubulin in mammalian development. *Trends Cell Biol.* **31**, 774–787 (2021).
42. F. Tissir, A. M. Goffinet, Shaping the nervous system: Role of the core planar cell polarity genes. *Nat. Rev. Neurosci.* **14**, 525–535 (2013).
43. J. B. Wallingford, B. Mitchell, Strange as it may seem: The many links between Wnt signaling, planar cell polarity, and cilia. *Genes Dev.* **25**, 201–213 (2011).
44. F. Tissir *et al.*, Lack of cadherins Celsr2 and Celsr3 impairs ependymal ciliogenesis, leading to fatal hydrocephalus. *Nat. Neurosci.* **13**, 700–707 (2010).
45. S. Ohata *et al.*, Loss of Dishevelleds disrupts planar polarity in ependymal motile cilia and results in hydrocephalus. *Neuron* **83**, 558–571 (2014).
46. D. K. Breslow *et al.*, A CRISPR-based screen for Hedgehog signaling provides insights into ciliary function and ciliopathies. *Nat. Genet.* **50**, 460–471 (2018).
47. H. R. Willsey *et al.*, Katanin-like protein Katnal2 is required for ciliogenesis and brain development in Xenopus embryos. *Dev. Biol.* **442**, 276–287 (2018).
48. E. Turk *et al.*, Zeta-tubulin is a member of a conserved tubulin module and is a component of the centriolar basal foot in multiciliated cells. *Curr. Biol.* **25**, 2177–2183 (2015).
49. S. Qiu *et al.*, ASD mutation of Katnal2 impairs ependymal ciliary motion and causes hydrocephalus. bioRxiv [Preprint] (2023). https://doi.org/10.1101/2023.07.03.547302 (Accessed 18 March 2024).
50. C. K. Tong *et al.*, Primary cilia are required in a unique subpopulation of neural progenitors. *Proc. Natl. Acad. Sci. U.S.A.* **111**, 12438–12443 (2014).
51. N. Kumamoto *et al.*, A role for primary cilia in glutamatergic synaptic integration of adult-born neurons. *Nat. Neurosci.* **15**, 399–405, s391 (2012).
52. M. R. Williams *et al.*, A retroviral CRISPR-Cas9 system for cellular autism-associated phenotype discovery in developing neurons. *Sci. Rep.* **6**, 25611 (2016).
53. S. Chen, B. Lee, A. Y. Lee, A. J. Modzelewski, L. He, Highly efficient mouse genome editing by CRISPR ribonucleoprotein electroporation of zygotes. *J. Biol. Chem.* **291**, 14457–14467 (2016).
54. H. Yang, H. Wang, R. Jaenisch, Generating genetically modified mice using CRISPR/Cas-mediated genome engineering. *Nat. Protoc.* **9**, 1956–1968 (2014).
55. J. Tyrone DeSpenza *et al.*, Dual impact of PTEN mutation on CSF dynamics and cortical networks via the dysregulation of neural precursors and their interneuron descendants. bioRxiv [Preprint] (2023). https://doi.org/10.1101/2023.03.18.533275 (Accessed 18 March 2024).
56. B. Zeng *et al.*, The single-cell and spatial transcriptional landscape of human gastrulation and early brain development. *Cell Stem Cell* **30**, 851–866.e857 (2023).
57. Z. Gu, R. Eils, M. Schlesner, Complex heatmaps reveal patterns and correlations in multidimensional genomic data. *Bioinformatics* **32**, 2847–2849 (2016).
58. H. Wickham, "ggplot2: Elegant graphics for data analysis" in *Use R!*, H. Wickham, Ed. (Springer International Publishing: Imprint: Springer, Cham, 2016), pp. 1 online resource (XVI, 260 pages 232 illustrations, 140 illustrations in color.
59. N. Chenouard *et al.*, Objective comparison of particle tracking methods. *Nat. Methods* **11**, 281–289 (2014).
60. I. F. Sbalzarini, P. Koumoutsakos, Feature point tracking and trajectory analysis for video imaging in cell biology. *J. Struct. Biol.* **151**, 182–195 (2005).
61. H. Li, R. Durbin, Fast and accurate short read alignment with Burrows-Wheeler transform. *Bioinformatics* **25**, 1754–1760 (2009).
62. R. Poplin *et al.*, Scaling accurate genetic variant discovery to tens of thousands of samples. bioRxiv [Preprint] (2018). https://doi.org/10.1101/201178 (Accessed 18 March 2024).
63. E. P. Garrison, G. T. Marth, Haplotype-based variant detection from short-read sequencing. arXiv: Genomics [Preprint] (2012). https://doi.org/10.48550/arXiv.1207.3907 (Accessed 18 March 2024).
64. K. Wang, M. Li, H. Hakonarson, ANNOVAR: Functional annotation of genetic variants from high-throughput sequencing data. *Nucleic Acids Res.* **38**, e164 (2010).
65. K. J. Karczewski *et al.*, The ExAC browser: Displaying reference data information from over 60 000 exomes. *Nucleic Acids Res.* **45**, D840–D845 (2017).
66. D. Taliun *et al.*, Sequencing of 53,831 diverse genomes from the NHLBI TOPMed Program. *Nature* **590**, 290–299 (2021).
67. K. J. Karczewski *et al.*, The mutational constraint spectrum quantified from variation in 141,456 humans. *Nature* **581**, 434–443 (2020).
68. Y. C. Wang *et al.*, Computational genomics in the era of precision medicine: Applications to variant analysis and gene therapy. *J. Pers Med.* **12**, 175 (2022).
69. R. Abagyan, M. Totrov, D. Kuznetsov, ICM–A new method for protein modeling and design: Applications to docking and structure prediction from the distorted native conformation. *J. Comput. Chem.* **15**, 488–506 (1994).